Automated long-range compensation of an rf quantum dot sensor

Joseph Hickie,[1,†] Barnaby van Straaten,[1,†] Federico Fedele,[1,†] Daniel Jirovec,[2] Andrea Ballabio,[3]
Daniel Chrastina,[3] Giovanni Isella,[3] Georgios Katsaros,[2] and Natalia Ares[4,*]

[1] *Department of Materials, University of Oxford, Oxford OX1 3PH, United Kingdom*
[2] *Institute of Science and Technology Austria, Am Campus 1, 3400 Klosterneuburg, Austria*
[3] *L-NESS, Physics Department, Politecnico di Milano, via Anzani 42, 22100 Como, Italy*
[4] *Department of Engineering Science, University of Oxford, Oxford OX1 3PJ, United Kingdom*

(Received 25 October 2023; revised 25 September 2024; accepted 1 November 2024; published 6 December 2024)

Charge sensing is a sensitive technique for probing quantum devices, of particular importance for spin-qubit readout. To achieve good readout sensitivities, the proximity of the charge sensor to the device to be measured is a necessity. However, this proximity also means that the operation of the device affects, in turn, the sensor tuning and ultimately the readout sensitivity. We present an approach for compensating for this crosstalk effect allowing for the gate voltages of the measured device to be swept in a 1-V × 1-V window while maintaining a sensor configuration chosen by a Bayesian optimizer. Our algorithm will hopefully be a major contribution to the suite of fully automated solutions required for the operation of large quantum device architectures.

DOI: 10.1103/PhysRevApplied.22.064026

I. INTRODUCTION

Radio-frequency (rf) charge sensing using a proximal quantum dot has become a ubiquitous technique for fast and sensitive measurements of quantum devices [1–6]. This technique is used for single-shot readout of spin qubits owing to its high sensitivity [7,8]. As devices scale to multiqubit architectures, the number of readout sensors per chip is bound to increase [9,10], making their manual tuning and optimization an increasingly time-consuming task. The high sensitivities provided by rf charge sensing rely on the high transconductance of the sensor dots, but the crosstalk between the device and the sensor dot results in this regime being quickly lost when sweeping the device gate voltages. To compensate for this crosstalk effect, existing techniques rely on digital feedback to maintain a constant current flowing through the sensor dot [11,12]. However, because these approaches do not necessarily maintain a high transconductance, crosstalk effects remain detrimental for the readout contrast. As a result, these methods are not able to keep a constant sensor sensitivity, especially when the device gate voltages are swept through ranges larger than 100-mV × 100-mV.

In this paper, we introduce an automated approach to find and maintain the high sensitivity of an rf sensor dot while sweeping across a large range of the gate-voltage space of a device. The algorithm is demonstrated in a hole-based Ge/SiGe heterostructure quantum dot array but is agnostic to the device material and geometry. Our algorithm employs Bayesian optimization to optimally tune the rf dot to a regime in which it is highly sensitive. Once the optimal readout contrast is found, virtual gates [13–17] are used to maintain the readout sensitivity in fast 100-mV × 100-mV measurement windows. This ac-based compensation is combined with a dc-based compensation algorithm to allow for the rf sensing of a stability diagram over 1-V × 1-V, in which we can distinguish more than 25 × 25 charge transitions, using a single sensing peak. Our compensation algorithm can be repeatedly recalibrated to arbitrarily extend this range, thus overcoming the limitation of the linear approximation required by the constant interaction model.

II. DEVICE AND MEASUREMENT SETUP

These experiments were performed in an electrostatically defined Ge/SiGe quantum dot (QD) fabricated in a similar manner to that described in Ref. [18]. Gates V_1–V_5 are used to define quantum dots in the main device, while gates V_{LB}, V_P, and V_{RB} define the charge sensor. Gates V_{LS} and V_{RS} separate the sensing dot from the device dots, and were both set to 1.8 V for this experiment. For readout, we

---

[*] Contact author: natalia.ares@eng.ox.ac.uk
[†] These authors contributed equally to this work.

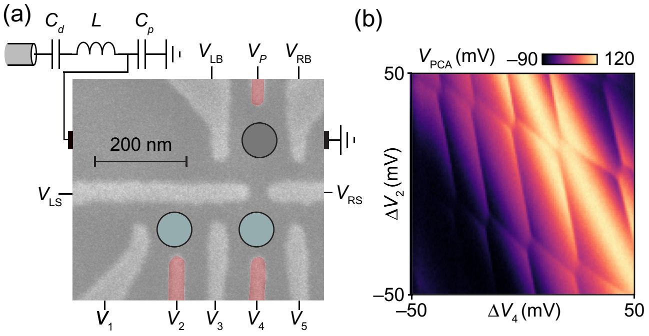

FIG. 1. (a) A scanning-electron-microscopy image of a device nominally identical to the one used in this experiment. The gate electrodes connected to microwave lines are color coded in pink. A bias tee combines a dc offset with the ac signal for the gates in red false color. (b) The demodulated signal from the rf quantum dot (rf QD) obtained by PCA when the device is in a double-dot regime. For a given point in gate-voltage space, we perform this two-dimensional (2D) measurement by ramping gates V_2 and V_4 in a raster pattern with an arbitrary waveform generator.

connected the ohmic of the charge sensor to an L-matching network with a 92-pF decoupling capacitor C_d, a 2.7-μH inductor L, and a parasitic capacitance C_p (see Fig. 1) [3]. We used a Zurich Instruments UHFLI to drive the circuit at a power of −90 dBm and demodulate the reflected signal.

The presented algorithm relies on fast two-dimensional (2D) measurements taken by ramping the voltage on gates V_2 and V_4 in a raster pattern using an arbitrary waveform generator (AWG) [19–21]. In these 2D measurement windows, the output waveforms are compensated to minimize the effect of distortion introduced by the filters as in Ref. [21]. We measured the demodulated in-phase (I) and out-of-phase (Q) components of the reflectometry signal from the rf-QD sensor for each pixel with an integration time of 1 μs (see Appendix A). To optimally capture both the I and Q components of the rf-QD signal, we use principal component analysis (PCA). The signal of the rf QD demodulated in this way is labeled V_{PCA} and corresponds to the first principal component of the measured data. For more details on the use of PCA, see Appendix D.

III. ALGORITHM

Our algorithm consists of two stages. The first stage optimally tunes the charge-sensor barriers (V_{LB} and V_{RB}) to achieve maximum sensitivity (Sec. III A). Optimal barriers are found when the impedance of the rf QD falls within a specific range such that the readout matching circuit has an impedance close to the $Z_0 = 50\,\Omega$ line impedance. We use a direct approach by defining a score function for the visibility of the charge sensor and then optimize it using Bayesian optimization.

The second stage is designed to maintain the tuning of the charge sensor while the device gate electrodes ($V_{1\text{–}5}$) are swept (Sec. III B). We compensate for this crosstalk by constructing virtual gates. These virtual gates include the plunger gate (V_P) of the charge sensor to compensate for the capacitive coupling between the gate electrodes of the device and the rf-QD sensor.

A. Optimally tuning charge-sensor tunnel barriers using Bayesian optimization

1. Variance-based score function for sensor visibility

With optimally tuned barriers, the difference between the reflected signal on and off a Coulomb peak is maximized, maximizing the height of the peaks and thus the readout sensitivity. Consequently, to optimize the sensitivity of the rf-QD sensor, we define a score function that maximizes the variance σ_M^2 of the voltage signal measured across a 2D charge-stability diagram. In the remainder of the paper, we refer to σ_M^2 as *the metric*.

To define the metric, we consider that the voltage value measured at each point in a 2D charge-stability diagram is made up by a true signal contribution and a noise contribution. The set of all voltage values M in a 2D measurement can thus be written as

$$M = S + N, \tag{1}$$

where S and N are, respectively, the sets of the signal and noise contributions of each point in a 2D measurement. In the following, we assume that at each measurement point, the noise contribution is drawn from a zero-mean Gaussian distribution with variance σ_N^2:

$$N \sim \mathcal{N}(\mu = 0, \sigma_N^2). \tag{2}$$

The variance of all the measured values in a 2D measurement scan, which is the value of the metric, is given by

$$\sigma_M^2 = \frac{1}{n}\sum_i m_i^2 - \frac{1}{n^2}\left(\sum_i m_i\right)^2, \tag{3}$$

where m_i is the measured value at each measurement point i and n is the number of measurement points. We have found that maximizing the metric defined in Eq. (3) is a fast and noise-resistant method for optimizing the visibility of the charge sensor (for further details, see Appendix B). This metric can be used to optimize not only the voltage tuning of the charge-sensor gates but also other parameters such as the rf frequency and power (see Appendix C).

To evaluate the score function, we initially take a fast 2D measurement as described in Sec. II and determine the variance of the data after projection onto the first principal component, Var(V_{PCA}). The variance of V_{PCA} is conceptually the same as considering the variance of the demodulated I component in a measurement where the phase of the reflectometry signal is optimally tuned (see Appendix D). If we only had access to the I component of the demodulated data, the score function could be evaluated by taking the variance in the I component. In this case, the phase would need to be optimized as an extra parameter in the subsequent Bayesian optimization.

2. Bayesian optimization of rf-QD sensor barrier gates

We aim to optimize our readout sensitivity by controlling the transparency of the tunnel barriers of the rf QD through gates V_{LB} and V_{RB}. For this purpose, we use a Bayesian optimizer [22] based on the upper-confidence-bound acquisition function. The optimizer proposes barrier gate voltages at which to evaluate the score function based on the posterior of a Gaussian process. We chose this approach over other common optimizers such as Nelder-Mead or Broyden–Fletcher–Goldfarb–Shanno (BFGS) due to the complex periodic nature of the optimization landscape given by the Coulomb peaks in the charge-stability diagrams of the rf QD. In Fig. 2(a), we show an example of the gate-voltage parameter space over which we optimize the barriers. Due to the periodicity of the sensor-dot Coulomb peaks, the score function contains several regions of low to high values that can easily trap these optimizers into local minima. Our Bayesian optimizer uses a Matérn 5/2 kernel with a length scale constrained to be greater than the Coulomb-peak spacing. This allows the model to only capture the large-scale variations of the score function, which is a more efficient strategy to find the global maximum. Each pixel in Fig. 2(a) is the variance of V_{PCA} measured across a fast 2D charge-stability measurement. To find the optimal barrier voltage, we could perform this measurement and take the values of V_{LB} and V_{RB} that result in $\max \mathrm{Var}(V_{\mathrm{PCA}})$. However, this is a very time-consuming approach, considering that this measurement is made up of 500 × 500 fast 2D measurements.

In our optimization approach, V_{LB} and V_{RB} are chosen by the optimizer. Initially, these voltages are chosen to explore the domain of the score function, building the Gaussian process model [see Fig. 2(b)]. Later iterations exploit the information in the model to converge on the global maximum [see Figs. 2(c) and 2(d)]. A sharp Coulomb peak, optimal for sensing, will thus be found at the coordinates in gate-voltage space that correspond to the global maximum of $\mathrm{Var}(V_{\mathrm{PCA}})$. Optimizing the barriers in this way requires approximately 100 fast 2D measurements.

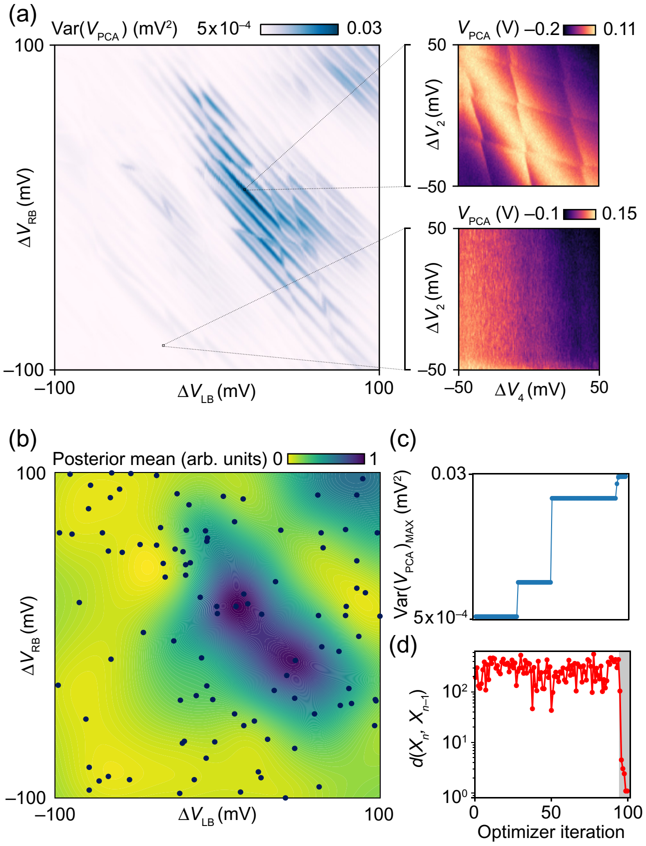

FIG. 2. (a) An example of the underlying score function over which we run the barrier optimization routine, representing the variance of V_{PCA} for a 200-mV × 200-mV window in the gate-voltage space given by the V_{LB} and V_{RB}. Each pixel in this scan represents the variance of V_{PCA} in a fast 2D measurement. The insets show examples of these measurements corresponding to two pixels with high and low variance. In regions in which the rf QD is sensitive, the variance is high (upper inset). In regions in which the rf QD is not sensitive, the variance is low, as the measurement is primarily noise (lower inset). (b) The posterior of a Gaussian process over a set of values of $\mathrm{Var}(V_{\mathrm{PCA}})$ from (a), marked by black points and chosen by the optimizer. The optimizer aims to find the maximum value of $\mathrm{Var}(V_{\mathrm{PCA}})$ in the gate-voltage window considered. (c) The maximum value of $\mathrm{Var}(V_{\mathrm{PCA}})$ that was found by the optimizer as a function of the number of iterations. As the optimization progresses, the optimal value of $\mathrm{Var}(V_{\mathrm{PCA}})$ increases. (d) The distance between sequential gate-voltage coordinates chosen by the optimizer. This distance decreases significantly for the last few iterations of the optimizer (gray area).

B. Compensating for crosstalk

In the previous stage of the algorithm, we have identified an optimal Coulomb peak for sensing. This Coulomb peak, present in the rf-QD sensor, is affected by the device gate voltages due to crosstalk. We aim to create virtual gates for the quantum dot device that allow us to move through the gate-voltage space of the devices while keeping the rf-QD Coulomb peak fixed in the 2D measurement window. We achieve this by compensating each device gate with a contribution from V_P. The resulting virtual gates V'_{1-5} would necessarily require V_P to act in the opposite direction to the device gate.

We begin by measuring the effect of each gate $V_{1\text{–}5}$ and V_P on the position of the rf-QD Coulomb peak in the 2D measurement window [see Figs. 3(a) and 3(b)]. This position (d) is defined to be the shortest distance from the lower-left corner of the 2D measurement to a linear regression fit of the rf-QD Coulomb peak (see Appendix E). We quantify the strength of the effect of the gate voltages on d as $\alpha_i = \Delta d_i/\Delta V_i$, where Δd_i is the change in d when the device gate voltage V_i is changed by a given ΔV. We can choose a gate-voltage range ΔV_i within which the values of α_i are constant, i.e., there is a linear dependence between d and V_i. If the full width of the rf-QD Coulomb peak is not visible in the 2D measurement window, the estimation of d becomes less reliable. An alternative approach to estimate the strength of the effect of the gate voltages on the position of the rf-QD Coulomb peak is to measure the finite-difference gradient of the peak edges for each of the gates $V_{1\text{–}5}$ and V_P (see Appendix F).

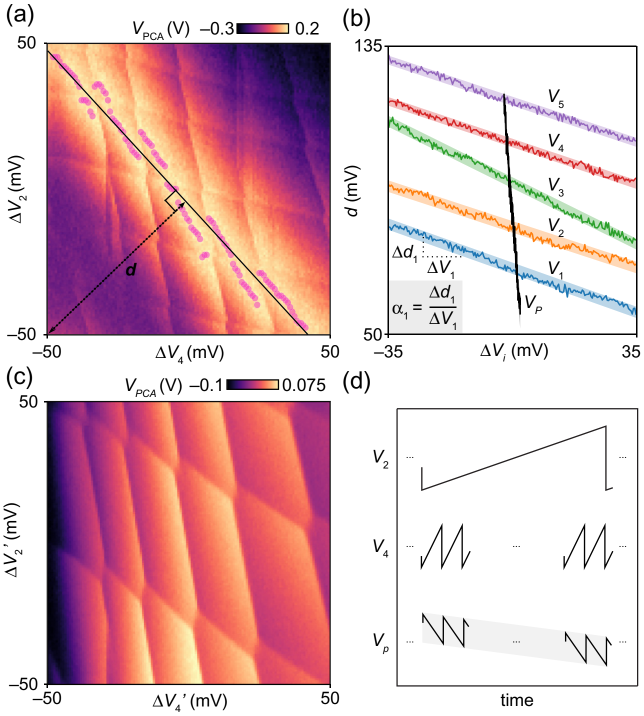

FIG. 3. (a) A 2D measurement window. The purple points identify the rf-QD Coulomb-peak maximum following the method described in Appendix E. The solid line is a regression fit through these points. The dashed line indicates d, the perpendicular distance of the rf-QD Coulomb peak to the lower-left corner of the 2D measurement window. (b) The values of the Coulomb-peak offset, d, as a function of changes in gate voltage for each of the gates of interest. Note the curves have been vertically offset to aid the reader. The plunger gate of the sensor, V_P, has the strongest gradient, as expected. (c) An example of a 2D measurement window after ac compensation. The uncompensated version can be found in Fig. 1(b). (d) The top two waveforms are schematics of the voltages applied to device gates to perform a 2D measurement window. The bottom waveform is the ac compensation voltage applied to V_P.

The strength of the compensating contribution from V_P in each virtual gate V_i' is given by a coefficient γ_i, given by $\gamma_i = \alpha_i/\alpha_P$, where α_P is the strength of the effect of V_P on d. The values of γ_i quantify the relative strength of each device gate compared to the strength of V_P on d. We would expect that γ_i is thus less than 1, since the plunger gate has a greater effect on the rf-QD Coulomb-peak position than any of the device gates.

The time taken to estimate γ_i depends on several parameters, including the resolution of the 2D measurement windows, the pixel integration time, the time it takes to sweep a gate voltage over ΔV_i, the processing speed of the computer, the number of device gates, and the number of sensors being compensated. In this setup, with five device gates and a single sensor plunger, the time taken to generate all the values of γ_i is approximately 10 s. This time could be reduced at the expense of noise robustness.

Our crosstalk compensation algorithm extracts the values of γ_i to achieve compensation over long-range device gate sweeps and for the gate sweeps within a 2D measurement window. We will refer to the former (latter) as dc (ac) compensation.

1. The dc compensation

As we perform a long-range device gate sweep, we navigate the stability diagram of the device. The position d of the rf-QD Coulomb peak in the measurement window changes as a result of this sweep. To compensate for a change in voltage ΔV on device gate i, the compensated device gate V_i' must increment the voltage on the sensor plunger gate V_P by a value opposite in sign and scaled by the relative strength of the compensating contribution, $-\gamma_i \Delta V$. This compensated device gate has a unit vector defined by

$$\hat{V}_i' \propto (\hat{V}_i - \gamma_i \hat{V}_P). \tag{4}$$

To generalize this concept, we first define an uncompensated virtual gate, which has an arbitrary direction in gate-voltage space spanned by $\{V_1, V_2, V_3, V_4, V_5, V_P\}$:

$$\hat{V}_{\text{arb}} \propto [\epsilon_1, \epsilon_2, \epsilon_3, \epsilon_4, \epsilon_5, 0]^T, \tag{5}$$

where ϵ_i represents the contribution of gate i to the virtual gate.

The corresponding compensated virtual gate is constructed by including the contributions to V_P:

$$\hat{V}_{\text{arb}}' \propto \left[\epsilon_1, \epsilon_2, \epsilon_3, \epsilon_4, \epsilon_5, -\sum_{i=1}^{5} \gamma_i \epsilon_i\right]^T. \tag{6}$$

2. The ac compensation

Within a measurement window, we can observe the rf-QD Coulomb peak due to the presence of crosstalk.

To compensate for this crosstalk, we create a waveform to compensate the fast sweeps that define the 2D measurement window. This third waveform is a linear combination of the two waveforms being used to generate the plunger fast sweeps [see Figs. 3(c) and 3(d)]:

$$V_P(t) = -\begin{bmatrix}\gamma_2\\ \gamma_4\end{bmatrix}\cdot\begin{bmatrix}V_2(t)\\ V_4(t)\end{bmatrix}, \qquad (7)$$

where $V_P(t)$, $V_2(t)$, and $V_4(t)$ are the ac components of the voltages applied to each of the three gates. V_P compensates for the cross-capacitive coupling between the device gates and the rf QD. In this way, we remove the gradients corresponding to the rf-QD Coulomb peak from the 2D-measurement-window background [see Fig. 1(d)]. This ac compensation approach is readily applicable to arbitrary pulses involving any number of device gates. Equation (7) is thus generalized by including additional time-dependent components scaled by the relevant γ value.

IV. RESULTS

As discussed in Sec. III B, a perfectly compensated gate V'_g would have an associated $\alpha_g = 0$, meaning that the Coulomb-peak offset d does not change as the compensated gate voltage V' is modified. We therefore measure the performance of our dc compensation algorithm by calculating the standard deviation of d, σ_d, as a function of the gate-voltage sweeps for three cases. In the first case, we generate uncompensated virtual gate-sweep directions as per Eq. (5). These virtual gate-sweep directions are constructed as an arbitrary linear combination of gates V_1–V_5. In the second case, we generate compensated virtual gates as per Eq. (6). In this case, the virtual gate-sweep directions are constructed as in the uncompensated case but a compensation term is included. Finally, we test the performance of each of the five compensated device gates as per Eq. (4). In this case, each virtual gate-voltage sweep is that of a single device gate and V_P.

For this performance test, a Coulomb peak was first selected by the Bayesian-optimization routine described in Sec. III A 2. The same peak was used for each of the benchmarking runs. To produce the arbitrary virtual gate directions, we generated 100 random vectors from the standard-normal distribution $\vec{\epsilon}_1, \ldots, \vec{\epsilon}_{100} \in \mathbb{R}^5$. These vectors were then used to create both uncompensated virtual gates and compensated virtual gates.

In Fig. 4(a), we show σ_d as a function of the length of the gate-voltage sweep, ΔV_g, for the three different sets of gate sweeps described above.

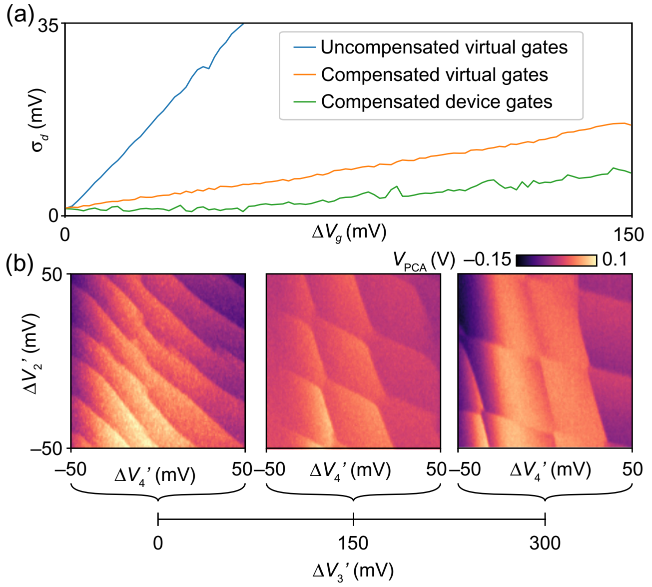

FIG. 4. (a) The standard deviation of the position of a Coulomb peak quantified by d, σ_d, as a function of the length of the gate-voltage sweep, ΔV_g, for uncompensated virtual gates [as per Eq. (5)] and for a different combination of gates in the compensated case [as per Eqs. (4) and (6)]. (b) Three 2D measurement windows for different gate-voltage configurations. These configurations are accessed by changing the value of the compensated-middle-barrier gate voltage, V'_3, by $\Delta V'_3$. Our compensation algorithm allows us to choose a Coulomb peak of our sensor dot and use it to explore the device gate-voltage space going from a single-dot to a double-dot regime. The ac compensation is applied for each of these 2D measurement windows.

Without dc compensation, at $\Delta V_g \approx 50$ mV, the Coulomb peak is no longer visible within the measurement window and σ_d saturates at 35 mV. Also, as we further increase ΔV_g, a different Coulomb peak becomes visible in the measurement window. With dc compensation, we observe that the algorithm drastically reduces σ_d over a gate-voltage range of 150 mV for both compensated device gates and compensated virtual gates. Ramping compensated device gates has a smaller effect on σ_d than ramping compensated virtual gates. This might have to do with nonlinearities in the effect of gate voltages that are accentuated in their combination. Our compensation algorithm applied to V_3 allows us to measure device operation regimes from single to double dot for a given Coulomb peak of the sensor dot [see Fig. 4(b)].

By combining both ac and dc compensation algorithms, we are able to produce large stability diagrams with clear charge transitions by maintaining offset of the chosen Coulomb peak for the sensor dot fixed. We demonstrate this by measuring 1000-mV × 1000-mV stability diagrams made up of 10 × 10 2D measurement windows. In Fig. 5(a), it is evident that when no compensation is applied, the visibility of charge transitions in the stability diagram varies significantly. The effect of crosstalk manifests in seven Coulomb-peak transitions of the sensor dot. With dc compensation applied, a Coulomb peak chosen by the Bayesian-optimization routine is used and its offset is kept fixed. The sensitivity of the sensor thus remains constant across different 2D measurement windows [see Fig. 5(b)]. Still, we observe a clear change in the sensitivity of the sensor within individual 2D measurement windows. Using both dc and ac compensation, the sensitivity 0f the sensor is kept mostly constant across the full stability diagram [see Fig. 5(c)]. This shows the extent of the capabilities of our compensation algorithm, with charge transitions being visible for almost a volt in each device-plunger direction.

V. DISCUSSION

We demonstrate how a quantum dot charge sensor can be quickly tuned and compensated for both ac and dc sweeps of the gate voltages of a device. In Fig. 5(c), we show that combining the ac and dc compensation algorithms results in a 1-V × 1-V stability diagram being measured while maintaining an optimal transconductance of the sensor dot found by a Bayesian optimizer.

The gate-voltage range within which this compensation approach can be applied is limited by the failure of the linearity assumption underlying the definition of virtual gates. The effectiveness of the compensation therefore reduces as the device gate voltages are swept far away from the gate-voltage location at which the virtual gates are calibrated. To overcome this challenge, the calibration process can be repeated with minimal time overheads.

Tuning of the gate voltages that control the tunnel barriers of the sensor dot takes approximately 10–60 s, depending on the optimization parameters. Similarly, the calibration of the virtual gates requires approximately 10 s per gate. In our device, this entire process can be completed in less than 2 min. Considering the construction of the posterior from the Gaussian processes, the additional time required to integrate our work into an experiment is in the order of 2–5 min. Once calibrated, the time overhead introduced by the dc compensation is shorter than approximately 20 ms. To put this in perspective, this is of the same order of magnitude as typical integration times per point in a standard lock-in or dc transport measurement in these devices. The ac compensation has no run-time overhead once the compensation waveforms are generated and uploaded to the AWG. This is because the raster scan and the compensation waveforms run in parallel. Importantly, this allows for the expansion of the gate-voltage range in which compensation can be applied, with negligible time overheads compared to typical tuning times for quantum dot devices. Additionally, the ac compensation can also be used for any type of fast 2D measurement, such as those involving qubit operations and interlaced pulse sequences. Aside from the ac compensation, we do not anticipate using our full algorithm during single-shot spin measurements. This is because these measurements are typically within the regime in which the linearity assumption for the virtual gates remains valid.

The effect of charge switches and gate-voltage drifts that change the sensitivity of the rf QD can be overcome by integrating a closed-loop feedback system for small measurement windows, such as those demonstrated in Refs. [11,12]. The approach that we present in this work naturally scales to device architectures with multiple sensors that can be compensated in parallel, as long as they can be simultaneously measured [10] via, e.g., frequency multiplexing [23]. The algorithm is fully automated and requires no human intervention and is therefore suitable for use in combination with other automated tuning procedures.

ACKNOWLEDGMENTS

We thank Nicholas Sim for providing help with the experiment and Sebastian Orbell for helpful discussions. This work was supported by the Royal Society, the Engineering and Physical Sciences Research Council (EPSRC) National Quantum Technology Hub in Networked Quantum Information Technology (Grant No. EP/M013243/1), Quantum Technology Capital (Grant No. EP/N014995/1), the EPSRC Platform Grant (Grant No. EP/R029229/1), the European Research Council (Grant Agreement No. 948932), the Scientific Service Units of the Institute of Science and Technology Austria through resources provided by the nanofabrication facility and, the FWF-I 05060 and HORIZON-RIA 101069515 projects.

APPENDIX A: FAST 2D MEASUREMENTS

We take the fast 2D measurements by applying sawtooth waveforms to gates V_2 and V_4 using a Tektronix AWG5024 arbitrary waveform generator. These pulses map out the voltage space in a raster pattern with a resolution of 128 × 128 pixels and are calibrated to be approximately 100 × 100-mV dc equivalent after filter compensation. At each pixel, we probe the state of the quantum dot charge sensor using rf reflectometry. The sensor is illuminated with an rf pulse generated by a Zurich UHFLI at 113.5 MHz at a power of −90 dBm, close to the resonant frequency of the readout circuit. The signal is demodulated by the same Zurich UHFLI. The X and Y components of the demodulated signal are sent to an Alazar ATS9440 digitizer, where the signal is integrated for 1 μs.

APPENDIX B: VARIANCE OF 2D MEASUREMENTS AS A SCORE FUNCTION

In this appendix, we justify the choice of σ_M^2 as a reliable parameter for a score function that maximizes the visibility of the charge sensor. In particular, we demonstrate that the metric is insensitive to various sources of measurement

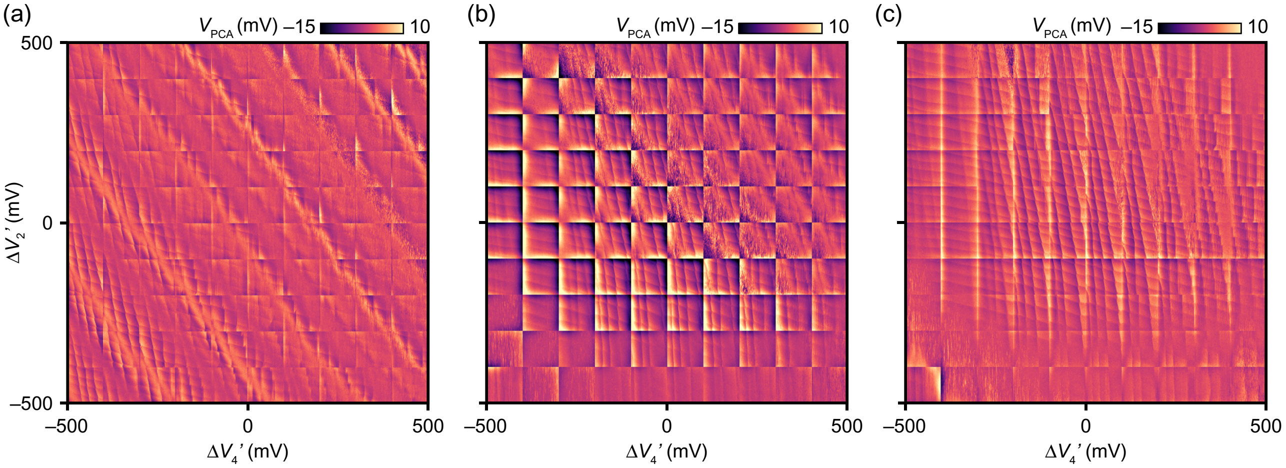

FIG. 5. A 1000-mV × 1000-mV mosaic of 2D measurement windows for three different cases: (a) without ac or dc compensation, (b) with just dc compensation for V_2 and V_4, and (c) with both dc and ac compensation for the same gates. The dc compensation maintains the sensor Coulomb-peak offset, d, fixed and the ac compensation makes charge transitions significantly clearer. The edges of the 2D measurement windows are still noticeable in (c) due to imperfections in the waveform compensation used to correct the distortion introduced by filters.

noise (such as charge and electric noise), especially for measurements with a large number of points.

To show this, we calculate the variance of the metric. Since the metric itself is defined as the variance of the voltage measured at each point in a 2D charge stability diagram (see Eq. (3)), we need to apply the variance formula for the propagation of errors:

$$\sigma_f^2 = \left(\frac{\partial f}{\partial x}\right)^2 \sigma_x^2 + \left(\frac{\partial f}{\partial y}\right)^2 \sigma_y^2 + \left(\frac{\partial f}{\partial z}\right)^2 \sigma_z^2 + \cdots , \tag{B1}$$

where σ_f^2 is the variance of the function f and σ_k^2 is the variance of variable k. To apply Eq. (B1) to Eq. (3), we first need the partial derivatives that make up Eq. (B1):

$$\frac{\partial \sigma_M^2}{\partial m_j} = \frac{2m_i}{n}\delta_{ij} - \frac{2}{n^2}\delta_{ij}\left(\sum_i m_i\right) \tag{B2}$$

$$= \frac{2m_j}{n} - \frac{2}{n^2}\left(\sum_j m_j\right), \tag{B3}$$

where j indexes the pixels in the measurement M. By Eq. (B1), the variance of the metric, σ_T^2, is given by:

$$\sigma_T^2 = \sum_j \left(\frac{\partial \sigma_M^2}{\partial m_j}\right)^2 \sigma_{m_j}^2, \tag{B4}$$

The variance of each pixel, $\sigma_{m_j}^2$, is given directly from the noise in the measurement and is therefore the same as the variance of N, σ_N^2. Therefore,

$$\sigma_T^2 = \sum_j \sigma_N^2 \left(\frac{2}{n}m_j - \frac{2}{n^2}\left(\sum_j m_j\right)\right)^2 \tag{B5}$$

$$= \sum_j \frac{4\sigma_N^2}{n^2}\left(m_j - \frac{1}{n}\sum_j m_j\right)^2 \tag{B6}$$

$$= \frac{4\sigma_N^2}{n^2}\sum_j (m_j - \bar{m})^2 \tag{B7}$$

$$= \frac{4\sigma_N^2}{n}\sum_j \frac{(m_j - \bar{m})^2}{n} \tag{B8}$$

$$= \frac{4\sigma_N^2}{n}\sigma_M^2. \tag{B9}$$

We can verify this result by simulation. To simulate the charge-sensing peak, we created a Lorentzian function centered around the diagonal of our simulated measurement and added noise. By repeatedly sampling the variance of this function, we obtained the variance of the variance, which gives the y axes in Fig. 6. We then varied the measurement noise scale and the number of points in the measurement. The results agree with those expected due to Eq. (B9), showing that the variance of this metric is small for a large number of pixels.

The result is that the noise sensitivity of the metric is extremely low, especially when a large number of points are used. Our measurements were 128 × 128, or 16 384 pixels. The noise of the metric scales with $1/n^2$, where n is

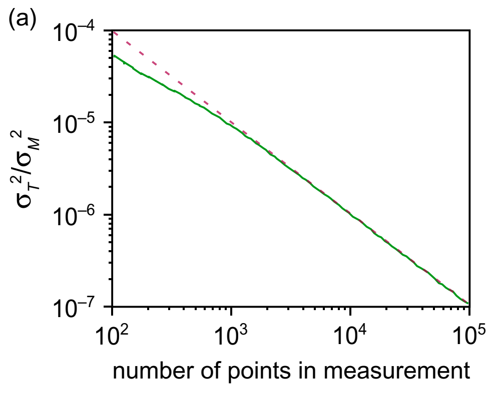

FIG. 6. The variance of the metric, σ_T^2 as a function of (a) the number of points in the measurement and (b) the measurement noise scale. Note that there were 10 000 points in the measurements for (b).

the number of pixels. The noise of this metric scales only linearly with the noise inherent in the measurement.

APPENDIX C: OPTIMIZING PARAMETERS USING VARIANCE

The tuning outlined in the paper typically uses the first principal component, which is the variance, of a 2D measurement to assess whether a regime is good or bad for charge sensing. A large variance means that the peak is tall and so highly sensitive. This technique is not restricted to tuning the plunger gate of the charge sensor to achieve an optimal position on a Coulomb peak; it is also useful for tuning any experimental parameter to optimize the reflectometry measurement signal-to-noise ratio.

As an example, consider a measurement that is designed to optimize the frequency of the reflectometry signal. If we sweep the frequency while watching the outcome of successive fast 100-mV × 100-mV measurements, we will see that the measurements go from just noise when the frequency does not align with the resonating frequency of the measurement circuit into signal when it is aligned and then back to noise when the frequency is too high (see Fig. 7). The frequency is optimal when the variance is maximized.

APPENDIX D: PRINCIPAL COMPONENT ANALYSIS

For two data-feature dimensions, x and y, the covariance matrix of the data is defined as

$$\Sigma = \begin{bmatrix} \sigma(x,x) & \sigma(x,y) \\ \sigma(y,x) & \sigma(y,y) \end{bmatrix}, \tag{D1}$$

where $\sigma(x,y)$ represents the covariance of x and y.

The paired eigenvectors and eigenvalues of the covariance matrix Σ represent the distribution of the variance of the data set in a new orthogonal basis composed of the eigenvectors. Each eigenvalue represents the variance of the data when projected onto its corresponding eigenvector.

For our measurements, the x and y dimensions are represented by the I (in-phase) and Q (out-of-phase) components of the reflected rf signal. We find the highest eigenvalue of the covariance matrix of these two data sets and take this to be the variance of our data for the score

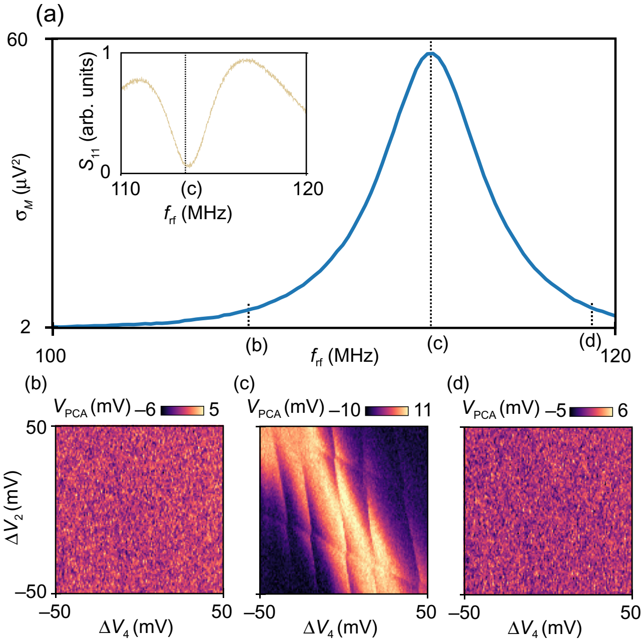

FIG. 7. (a) The variance of a 100-mV × 100-mV measurement at a fixed point in voltage space as a function of the reflectometry frequency. As the frequency approaches the resonant frequency of the readout circuit, the visibility of the charge sensor increases, leading to an increase in variance. The inset shows the cavity S_{11} response as a function of the frequency for comparison. (b)–(d) Examples of these measurements at different rf frequencies.

function defined in Sec. III A 1. The paired eigenvector is known as the first principal component of the data.

The eigenvector is a vector in IQ space with an equation $y = mx + c$. We subtract the mean from the data, so the best-fit line, which is exactly equivalent to the eigenvector with the highest corresponding eigenvalue, will also have zero mean in both dimensions, meaning that its equation simplifies to $y = mx$. The gradient is therefore $m = y/x$, representing an angle of $\arctan y/x$. The phase of a data point in XY space is also $\phi = \arctan y/x$ [6], so the angle of the best-fit line will be at the same angle as that represented by the phase. Projecting the data onto the first principal component is therefore identical to optimally tuning the phase for a given measurement.

APPENDIX E: FITTING LINE TO COULOMB-PEAK MEASUREMENT

This appendix describes how we fit a line to the Coulomb peak for fast 2D measurements as described in Sec. II [see, e.g., Fig. 3(a)].

Initially, two linear models are generated from the measurement: the first contains the pixels with the maximum value in each column and the second with the maximum value in each row. We then generate a line fit for both sets and keep the set with the fit that has the largest r^2 value. This model-selection routine stabilizes the following part of the algorithm. The selected peak line now lies across the top of the Coulomb peak in the charge sensor and has the equation $ax + by + c = 0$ [Fig. 3(a), solid black line]. To obtain a measure of the position of the peak line, we calculate the shortest distance from it to the origin of the measurement (x_0, y_0) [Fig. 3(a), dashed black line] and name this distance d. The point on the peak line closest to the origin is at (m, n) and the line from here to the origin is perpendicular to the peak line. The distance from (x_0, y_0) to (m, n), is

$$d = \frac{|ax_0 + by_0 + c|}{\sqrt{a^2 + b^2}}, \tag{E1}$$

and since $(x_0, y_0) = (0, 0)$ in pixel space,

$$d = \frac{|c|}{\sqrt{a^2 + b^2}}. \tag{E2}$$

APPENDIX F: FINITE-DIFFERENCES GRADIENT METHOD FOR OBTAINING COUPLING STRENGTHS

We can obtain the relative coupling strengths of each gate on the potential of the rf QD by measuring the gradient of a Coulomb peak as a function of the voltage of each gate. A Coulomb peak is approximately Lorentzian and therefore does not have a constant gradient. For a local compensation approach, we can approximate the gradient using finite-difference methods.

We initially tune to the side of a Coulomb peak in the rf-QD sensor. For each gate, we measure at two gate voltages, $V_{\text{gate}} - (\delta V_{\text{in}}/2)$ and $V_{\text{gate}} + (\delta V_{\text{in}}/2)$, and calculate the finite-difference gradient by $\delta_h[V_{\text{gate}}] = \delta V_{\text{out}}/\delta V_{\text{in}}$. At each of the two gate voltages, we measure N samples and calculate the gradient based on the averages of these samples (see Fig. 8).

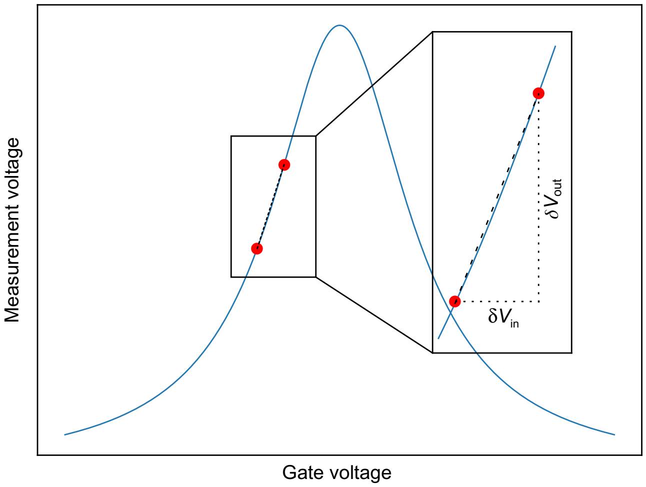

FIG. 8. A demonstration of the finite-differences method for obtaining the gradient of the sensor peak. N samples are taken at each of the two positions indicated by the red points and the average of each of these two sets is used to calculate the gradient $\delta V_{\text{out}}/\delta V_{\text{in}}$.

[1] R. J. Schoelkopf, P. Wahlgren, A. A. Kozhevnikov, P. Delsing, and D. E. Prober, The radio-frequency single-electron transistor (rf-SET): A fast and ultrasensitive electrometer, Science **280**, 1238 (1998).

[2] C. Barthel, M. Kjærgaard, J. Medford, M. Stopa, C. M. Marcus, M. P. Hanson, and A. C. Gossard, Fast sensing of double-dot charge arrangement and spin state with a radio-frequency sensor quantum dot, Phys. Rev. B **81**, 161308 (2010).

[3] N. Ares, F. J. Schupp, A. Mavalankar, G. Rogers, J. Griffiths, G. A. Jones, I. Farrer, D. A. Ritchie, C. G. Smith, A. Cottet, G. A. Briggs, and E. A. Laird, Sensitive radio-frequency measurements of a quantum dot by tuning to perfect impedance matching, Phys. Rev. Appl. **5**, 1 (2016).

[4] T. Müller, B. Küng, S. Hellmüller, P. Studerus, K. Ensslin, T. Ihn, M. Reinwald, and W. Wegscheider, An *in situ* tunable radio-frequency quantum point contact, Appl. Phys. Lett. **97**, 202104 (2010).

[5] A. Noiri, K. Takeda, J. Yoneda, T. Nakajima, T. Kodera, and S. Tarucha, Radio-frequency-detected fast charge sensing in undoped silicon quantum dots, Nano Lett. **20**, 947 (2020).

[6] F. Vigneau, F. Fedele, A. Chatterjee, D. Reilly, F. Kuemmeth, M. F. Gonzalez-Zalba, E. Laird, and N. Ares, Probing quantum devices with radio-frequency reflectometry, Appl. Phys. Rev. **10**, 021305 (2023).

[7] A. West, B. Hensen, A. Jouan, T. Tanttu, C. H. Yang, A. Rossi, M. F. Gonzalez-Zalba, F. Hudson, A. Morello, D. J. Reilly, and A. S. Dzurak, Gate-based single-shot readout of spins in silicon, Nat. Nanotechnol. **14**, 437 (2019).

[8] M. Hogg, P. Pakkiam, S. Gorman, A. Timofeev, Y. Chung, G. Gulati, M. House, and M. Simmons, Single-shot readout of multiple donor electron spins with a gate-based sensor, PRX Quantum **4**, 010319 (2023).

[9] S. G. Philips, M. T. Madzik, S. V. Amitonov, S. L. de Snoo, M. Russ, N. Kalhor, C. Volk, W. I. Lawrie, D. Brousse, L. Tryputen, P. Brian, A. Sammak, M. Veldhorst, G. Scappucci, and L. M. K. Vandersypen, Universal control of a six-qubit quantum processor in silicon, Nature **609**, 919 (2022).

[10] F. Fedele, A. Chatterjee, S. Fallahi, G. C. Gardner, M. J. Manfra, and F. Kuemmeth, Simultaneous operations in a two-dimensional array of singlet-triplet qubits, PRX Quantum **2**, 040306 (2021).

[11] C. H. Yang, W. H. Lim, F. A. Zwanenburg, and A. S. Dzurak, Dynamically controlled charge sensing of a few-electron silicon quantum dot, AIP Adv. **1**, 042111 (2011).

[12] T. Nakajima, Y. Kojima, Y. Uehara, A. Noiri, K. Takeda, T. Kobayashi, and S. Tarucha, Real-time feedback control of charge sensing for quantum dot qubits, Phys. Rev. Appl. **15**, 1 (2021).

[13] T. Hensgens, T. Fujita, L. Janssen, X. Li, C. J. Van Diepen, C. Reichl, W. Wegscheider, S. Das Sarma, and L. M. Vandersypen, Quantum simulation of a Fermi-Hubbard model using a semiconductor quantum dot array, Nature **548**, 70 (2017).

[14] T. Botzem, M. D. Shulman, S. Foletti, S. P. Harvey, O. E. Dial, P. Bethke, P. Cerfontaine, R. P. McNeil, D. Mahalu, V. Umansky, A. Ludwig, A. Wieck, D. Schuh, D. Bougeard, A. Yacoby, and H. Bluhm, Tuning methods for semiconductor spin qubits, Phys. Rev. Appl. **10**, 1 (2018).

[15] C. Volk, A. M. Zwerver, U. Mukhopadhyay, P. T. Eendebak, C. J. van Diepen, J. P. Dehollain, T. Hensgens, T. Fujita, C. Reichl, W. Wegscheider, and L. M. Vandersypen, Loading a quantum-dot “Qubyte” based register, npj Quantum Inf. **5**, 1 (2019).

[16] A. R. Mills, D. M. Zajac, M. J. Gullans, F. J. Schupp, T. M. Hazard, and J. R. Petta, Shuttling a single charge across a one-dimensional array of silicon quantum dots, Nat. Commun. **10**, 1063 (2019).

[17] F. Ansaloni, H. Bohuslavskyi, F. Fedele, T. Rasmussen, B. Brovang, F. Berritta, A. Heskes, J. Li, L. Hutin, B. Venitucci, B. Bertrand, M. Vinet, Y.-M. Niquet, A. Chatterjee, and F. Kuemmeth, Gate reflectometry in dense quantum dot arrays, New J. Phys. **25**, 033023 (2023).

[18] D. Jirovec, A. Hofmann, A. Ballabio, P. M. Mutter, G. Tavani, M. Botifoll, A. Crippa, J. Kukucka, O. Sagi, F. Martins, J. Saez-Mollejo, I. Prieto, M. Borovkov, J. Arbiol, D. Chrastina, G. Isella, and G. Katsaros, A singlet-triplet hole spin qubit in planar Ge, Nat. Mater. **20**, 1106 (2021).

[19] J. Stehlik, Y.-Y. Liu, C. M. Quintana, C. Eichler, T. R. Hartke, and J. R. Petta, Fast charge sensing of a cavity-coupled double quantum dot using a Josephson parametric amplifier, Phys. Rev. Appl. **4**, 014018 (2015).

[20] F. J. Schupp, F. Vigneau, Y. Wen, A. Mavalankar, J. Griffiths, G. A. Jones, I. Farrer, D. A. Ritchie, C. G. Smith, L. C. Camenzind, L. Yu, D. M. Zumbühl, G. A. Briggs, N. Ares, and E. A. Laird, Sensitive radiofrequency readout of quantum dots using an ultra-low-noise SQUID amplifier, J. Appl. Phys. **127**, 244503 (2020).

[21] B. van Straaten, F. Fedele, F. Vigneau, J. Hickie, D. Jirovec, A. Ballabio, D. Chrastina, G. Isella, G. Katsaros, and N. Ares, All rf-based tuning algorithm for quantum devices using machine learning, ArXiv:2211.04504.

[22] F. Nogueira, Bayesian optimization: Open source constrained global optimization tool for PYTHON, 2014, https://github.com/bayesian-optimization/BayesianOptimization.

[23] A. Ruffino, T.-Y. Yang, J. Michniewicz, Y. Peng, E. Charbon, and M. F. Gonzalez-Zalba, A cryo-CMOS chip that integrates silicon quantum dots and multiplexed dispersive readout electronics, Nat. Electron. **5**, 53 (2022).